# IRONSperm swimming by rigid-body rotation versus transverse bending waves influenced by cell membrane charge

Magdanz, Veronika; Klingner, Anke; Abelmann, Leon; Khalil, Islam S.M.

**DOI**
10.1007/s12213-023-00158-5

**Publication date**
2023

**Document Version**
Final published version

**Published in**
Journal of Micro-Bio Robotics

**Citation (APA)**
Magdanz, V., Klingner, A., Abelmann, L., & Khalil, I. S. M. (2023). IRONSperm swimming by rigid-body rotation versus transverse bending waves influenced by cell membrane charge. *Journal of Micro-Bio Robotics*, *18*(1-2), 49-60. https://doi.org/10.1007/s12213-023-00158-5

Journal of Micro and Bio Robotics
https://doi.org/10.1007/s12213-023-00158-5

RESEARCH

# IRONSperm swimming by rigid-body rotation versus transverse bending waves influenced by cell membrane charge

**Veronika Magdanz**[1,2] · **Anke Klingner**[3] · **Leon Abelmann**[4,5] · **Islam S.M. Khalil**[6]

Received: 9 November 2022 / Revised: 27 April 2023 / Accepted: 6 May 2023

## Abstract

Cell membrane potential affects the electrostatic self-assembly of magnetizable nanoparticles around the flagellum of sperm cells, leading to the formation of biohybrid microrobots (i.e., IRONSperm) with various bending stiffness. Here we explain the influence of bull sperm cell membrane potential on the formation of two types of IRONSperm samples that are produced by electrostatic self-assembly. The first type is a proximal-coated soft body with nanoparticles concentrated on the head to maintain high flexibility of the flagellum and create a passively propagating transverse bending wave under the influence of an external rotating magnetic field. The second type is a rigid-body with nanoparticles approximately uniformly distributed along the length to provide arbitrary geometry that maintains a constant chiral shape and propel by rotation about its long axis. We present a magneto-elastohydrodynamic model to predict the swimming speed at low Reynolds number for rigid IRONSperm with arbitrary shapes, and show that decreasing the bending stiffness allows the model to capture the behavior of its soft counterpart. While the response of a rigid chiral IRONSperm is distinguished by a greater swimming speed with a smooth decay with frequency, the benefit of a soft flagellum in certain scenarios would present a much smaller range of frequencies for wireless actuation.

**Keywords** Biohybrid · Magnetic · Microrobots · Nanoparticles · Sperm cells

## 1 Introduction

There is an increasing need for wireless autonomous microrobots that can perform important tasks such as sensing, diagnosis [1, 2], locomotion, actuation [3], and localized drug delivery [4]. A challenge with these active systems is the bulk fabrication of stimuli-responsive biocompatible materials at the micro scale; loading with concentrated doses of drugs and swimming efficiently at low Reynolds number ($Re$) hydrodynamics. One solution for the fabrication of such systems is a biohybrid approach, in which synthetic and biological components are self-assembled through electrostatic interactions into biohybrid microrobots with novel properties. In this framework, motile or immotile cells are integrated with inorganic components, that are developed by synthesis or microfabrication. Propulsive thrust can be directly produced by motile organisms [5] or by external magnetic fields. In these biohybrid active systems, the inorganic component can provide additional functions (e.g., magnetic moment for wireless actuation [6], photothermal therapy [8], and contrast agents for noninvasive localization [9, 10]) that cannot be incorporated to the organisms through genetic engineering. The use of immotile organisms as elements for the propagation of mechanical waves makes the biohybrid microrobots less sensitive to chemical and biological conditions (e.g., $p$H, nutritional levels, temperature, lifetime of the cells) in the environment.In previous studies, our group developed the so-called *IRONSperm* by self-assembly between magnetic nanoparticles and bovine spermatozoa, leading to sperm-templated magnetic microrobots. The self-assembly occurs based on electrostatic interactions between mostly negatively charged sperm membrane and positively charged magnetic nanoparticles. These magnetically functionalized spermatozoa are rendered immotile after this process and external rotating magnetic fields are then utilized to actuate these flexible biohybrid microrobots.[6] Although maximum robustness to biological conditions can be obtained from the integration of immotile cells and

---

✉ Veronika Magdanz
veronika.magdanz@uwaterloo.ca

✉ Islam S.M. Khalil
i.s.m.khalil@utwente.nl

Extended author information available on the last page of the article

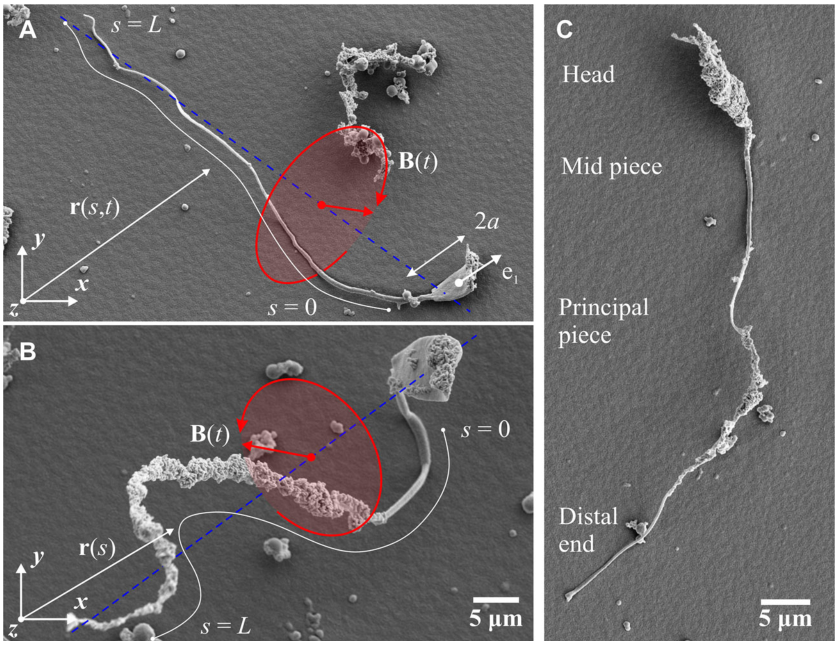

**Fig. 1** The surface charge, $q_s(s)$, of the organic body varies along the arclength, $s \in [0, L]$, and across sperm cells, and yields intrinsic variable stiffness between samples.The blue dashed lines represent the long axis of the cell. (A) Nanoparticle concentration small enough to provide a magnetic moment to bull sperm cells enables them to swim using propagating transverse waves in a rotating magnetic field. (B) Nanoparticle concentration large enough to provide rigid biohybrid structure allows for swimming by rigid-body rotation under the influence of a rotating magnetic field, $\mathbf{B}(t)$. (C) Morphological segments of the spermatozoon with head, mid piece, principal piece and distal end

inorganic components (Fig. 1(A)), the variation between the produced samples is significant, in terms of geometry, elasticity [11], and magnetization [12], for three key reasons. First, the bending stiffness of each cellular segment of the sperm cell (head, mid piece, principal piece and distal end, see Fig. 1C) is distinctive due to their specific design and sperm bauplan[13]. Second, there is a variation of stiffness of the flagella influenced by the level of adenosine triphosphate (ATP), Mg, and other molecular levels inside the cell [22]. This leads to an intrinsic variation of bending stiffness. Third, the membrane composition affects the surface charge, thereby changing the particle-membrane electrostatic interactions. Particularly, in spermatozoa, the membrane charge varies with the maturation state of the cell. This property leads to a variation of particle load on the flagella, also influencing the stiffness of the biohybrid microrobot. The cell membrane potential shows a significant difference between samples, leading to sporadically attached nanoparticles along the flagellum (Fig. 1(B)).

Microfabrication technologies allow us to add a specific structure, and thereby providing functions to a microorganism. Plant-based biotemplated magnetically propelled helical microswimmers have been fabricated using spiral water-conducting vessels of different plants and the sequential deposition of Ti and Ni layers enables rotation in human serum under the influence of a time-periodic magnetic field [14]. Similarly, Kamata et al. have presented a biotemplating process onto *Spirulina* surface to fabricate metal microcoils [15], using an electroless plating technique, which can generate smooth metal layers selectively. The results of this work suggest that mass production of helical geometries with magnetic functionality is possible. However, when selecting the material deposited on the *Spirulina* template, the selection of drug loading will be limited to surface functionalization and coating. Dip-coating is an alternative approach to add several functionalities to an organic body in a single-step fabrication process. Yan et al. have fabricated biohybrid magnetic microrobots by integrating *Spirulina* microalgae via a facile dip-coating process in a magnetite (i.e., $Fe_3O_4$) suspensions [9]. The resulting microrobot exhibits intrinsic fluorescence, natural degradability, and desirable cytotoxicity. These microrobots can swim or roll on a nearby solid boundary by rigid-body rotation using an external magnetic field [6]. Similarly, it has been shown that sperm cells can be coated by magnetizable nanoparticles and achieve drag-based propulsion in low-*Re* using rotating magnetic fields. Such microrobots are promising candidates for drug delivery and in vivo imaging of spermatozoa. This self-assembly based fabrication of magnetic sperm-templated microrobots results in a variety of swimmers, which were characterized and categorized in a previous study [12]. In this article, we investigate the underlying reasons for the differences in particle coating and the resulting flexibility of the magnetic swimmers. The membrane charge of the cells significantly affects the nanoparticle coating, resulting in *at least* two swimming modes using drag-based propulsion: swimming by rigid-body rotation and swimming by transverse bending wave propagating along a flexible tail, both under the influence of a rotating magnetic field. We focus on the important effect of the surface charge of the cell membrane on the mechanical and magnetic properties of nanoparticle-coated sperm cells (i.e., IRONSperm). Further, we model the influence of these properties on the deformation of IRONSperm. A three-dimensional (3-D) magneto-elastohydrodynamic model enables us to determine the swimming speed and propulsive thrust of rigid bodies with arbitrary initial deformations and show that decreasing the bending stiffness allows the model to capture the behavior of the soft IRONSperm.

## 2 Influence of cell membrane potential on propulsion mechanisms

The self-assembly of spermatozoa with surface charge $q_\mathrm{s}(s)$ and rice grain-shaped magnetic particles with charge $q_\mathrm{p}$ relies on the electrostatic interaction between the negatively-charged areas of the cell membrane and positively charged nanoparticles, $q_\mathrm{p}q_\mathrm{s}(s)/(4\pi\epsilon_0 z^2)$, where $\epsilon_0$ and $z$ are the permittivity and closest separation distance between particles and a point along the arclength $s$, respectively. This interaction has led to a variety of sperm-particle constructs in terms of surface coverage and location of the magnetizable nanoparticles, resulting in a wide variety of responses to the rotating magnetic field [12, 19]. The elongated shape of the nanoparticles contributes to an enhanced overall magnetization due to their alignment. Note that spherical particles have been tested previously and did not result in a comparable magnetic moment to that of the rice-shaped particles. The cell membrane potential influences the resulting propulsion mechanism of IRONSperm. In order to understand this behavior, we look into the peculiarities of spermatozoa's membranes and analyze its influence on the membrane charge.

### 2.1 Membrane charge of IRONSperm

One reason for the different coverage of rice grain-shaped magnetic particles on the sperm membranes can be seen in the variation of charges across the membrane. The cell membrane's main building block is a double lipid membrane that is characterized by negative surface charges on the hydrophilic head facing outwards. The membrane charges are governed by the decoration of the membrane with carbohydrates, proteins and other intercalated macromolecules in the membrane (Fig. 2). One particular property of sperm membranes is that their composition changes during the lifetime of the spermatozoa. IRONSperm were fabricated by electrostatic self-assembly between rice-shaped 100 nm wide iron oxide nanoparticles and bull spermatozoa, as previously reported [27].The size of bovine spermatozoa is about 70 μm in length with a 1 μm wide, 60 μm long flagellum and head dimensions of 10 μm×5 μm×1 μm. Figure 2A illustrates the changes sperm cells undergo in their three main developmental stages [7]. During the first stage, the sperm cell's specific morphology is developed by changing from round spermatogonia to flagellated cells with an elongated head, in which the genetic information is stored in the nucleus (black circle). Next, during the epididymal maturation, the sperm's membrane is exposed to the complex medium of the epididymis and gains many molecules that are important for fertilization while also taking up molecules that prevent premature capacitation (Fig. 2Aiii). In the female reproductive tract, the sperm cells gain full functional competence (Fig. 2Aiv). The inhibitory molecules are removed and cholesterol is released. The membrane is remodelled so that fusion with the egg can occur. Finally, the acrosome fuses with the sperm membrane to release enzymes that support the penetration of the zone pellucida (Fig. 2Av). In particular, cholesterol ($C_{27}H_{46}O$) is abundantly embedded in the membrane and released upon maturation. The presence of cholesterol affects the membrane fluidity, facilitates cell signaling and helps maintain the integrity of these membranes. Cholesterol can make up nearly half of the membrane by molecular number. It is smaller and weighs less than other molecules in the cell membrane, so that it makes up a lesser proportion of the cell membrane's mass, approximately 20%. Cholesterol adds firmness and integrity to the plasma membrane. The presence of cholesterol reduces indirectly the negative surface charge of membranes, by allowing sodium ion (Na+) binding and thus turning it more neutral [21].

### 2.2 Charge distribution and bending stiffness

The heterogeneous membrane structure is important to regulate different cell functions such as protein uptake or signalling. The changes in membrane composition are driven by maturation processes which prepare the cell for the final step of fusion with the oocyte at the time of fertilization. Overall, the net charge of most cells is negative, $\langle q_s(s)\rangle < 0$, however this can vary from cell to cell. Currently, the state-of-the-art research methods in biology do not offer any quantitative analysis of sperm membrane charge distribution. Initial studies give insights on how the net charge of biological cells can be measured, e.g. by electrophoretic mobility of cells. This approach works well for circular cells with a form factor close to 1. The form factor is the ratio of the circumference to the area normalized to a circle and describes the shape of a cell. The cell compactness has the lowest value of 1 when the outline of the object is a circle and increases as the cell increases in length. When the shape factor of the cells is much higher 1, such as in the case of spermatozoa with a length of over 60 μm and diameter of 1 μm of the tail and 10 μm × 5 μm × 1 μm head size, this technique does not give reliable results. Spermatozoa with their elongated, flagellated morphology do not provide accurate data when measuring their electrophoretic mobility [16]. Another approach was conducted recently by using the attachment of particles with known charge to sperm cells by electrostatic interactions to create a charge map of sperm cells [19]. Simi-

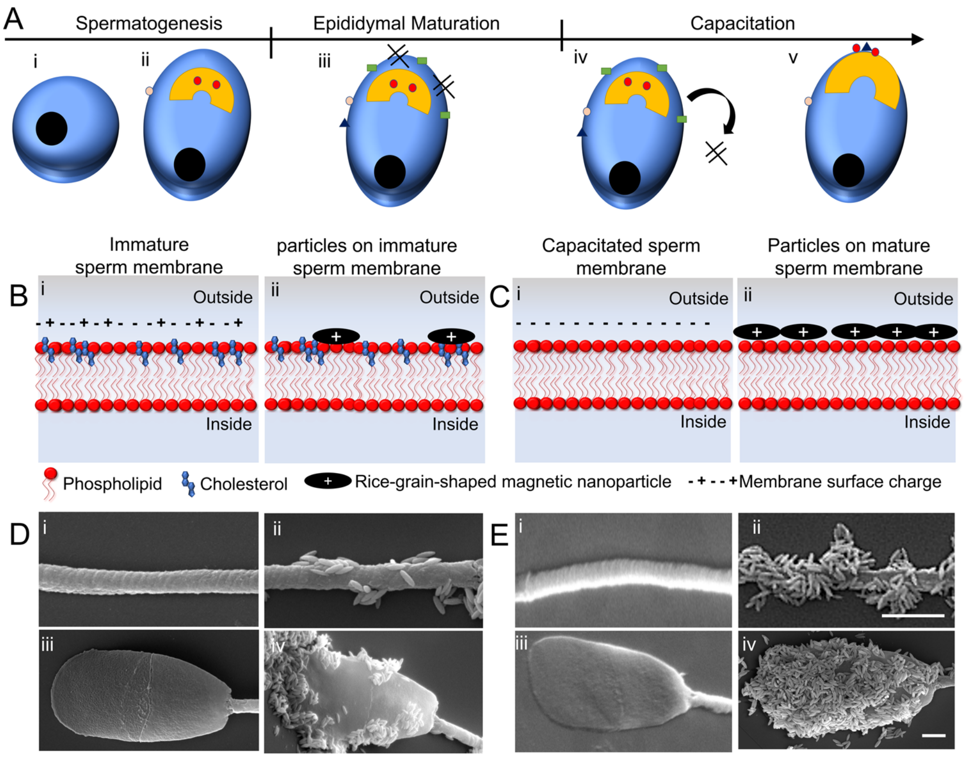

**Fig. 2** The magnetic nanoparticle coating of IRONSperm is governed by the charge-distribution and composition of the membrane. (A)Changes in sperm head surface throughout the 3 stages of sperm maturation. Adapted from [7] (Ai) Spermatogenesis converts round spermatogonia into morphologically mature sperm. (Aii) Expression of proteins on sperm surface, formation of acrosomal matrix (yellow). (Aiii) During epididymal maturation, a large number of proteins and molecules crucial for fertilization are embedded in the membrane. (Aiv) Cholesterol (green) efflux and loss of inhibitory molecules result in hyperactive motility and sperm's ability to bind to egg. (Av) Acrosomal matrix (yellow) fuses with sperm membrane required for adhesion to egg.(B) Cholesterol(blue), among other components, is integrated in the membrane. (Bi) Immature cells consist of a negatively-charged lipid bilayer with a large portion of cholesterol which shifts the net membrane charge, $q_s$, to more neutral. (B-ii) Such cells, when exposed to positively charged nanoparticles create IRONSperm with few particles due to low electrostatic binding sites on their surface. (C-i) When sperm cells undergo the maturation process called capacitation, they shed cholesterol from the membrane which shifts the net charge of the membrane to a more negative value. (C-ii) This results in IRONSperm with high coverage of particles, due to strong electrostatic interactions. Scanning electron microscopic images of flagella membrane before particles attachment (D-i), (E-i), with few particles bound (D-ii) and high load of particles (E-ii). Electron microscopic images of sperm heads before particle attachment (D-iii), (E-iii), with few particles in case of low negative charge (D-iv) and highly negative charge (E-iv). A sperm sample usually has a population of immature and mature cells and the resulting IRONSperm population displays cells with full or partial coverage of nanoparticles. Scale bars are 1 µm

larly, this method only provides an estimate of the membrane charge distribution and will be challenging to investigate, given the fluidic and dynamic properties of live spermatozoa. The control over the charge of sperm cells has not been explored yet. Shedding of proteins or lipids (Cholesterol) from the sperm membrane during capacitation is known to have an effect on the sperm charge. With this information, it might be possible to alter the sperm membrane in a qualitative manner in future studies. Besides the composition of the lipid raft of the membrane, external conditions also play a role such as $p$H, temperature, and ionic concentrations [17]. The influence of the environmental factors are avoided by washing the cells in de-ionized water before incubating them with the positively charged magnetic nanoparticles. Thus, when exposed to positively charged nanoparticles, the amount of particles that electrostatically bound to the surface correlates with the initial net negative charge of the cell at the point of charge equilibrium. This results in a relatively higher or lower concentration on the surface. A high particle concentration results in rigid IRONSperm (Figs. 2Cii and Eii and iv), while a low concentration, scattered particle binding leads to flexible IRONSperm (Fig. 2Bii and Dii and iv). A huge variety of IRONSperm are formed, depending on the sperm membrane charge distribution. Especially the particle coating on the flagella will have an effect on the bending stiffness of the resulting swimmer. In a recent study we investigated the passive bending stiffness of the magnetic nanoparticle-coated flagella of bull sperm cells by using a contactless

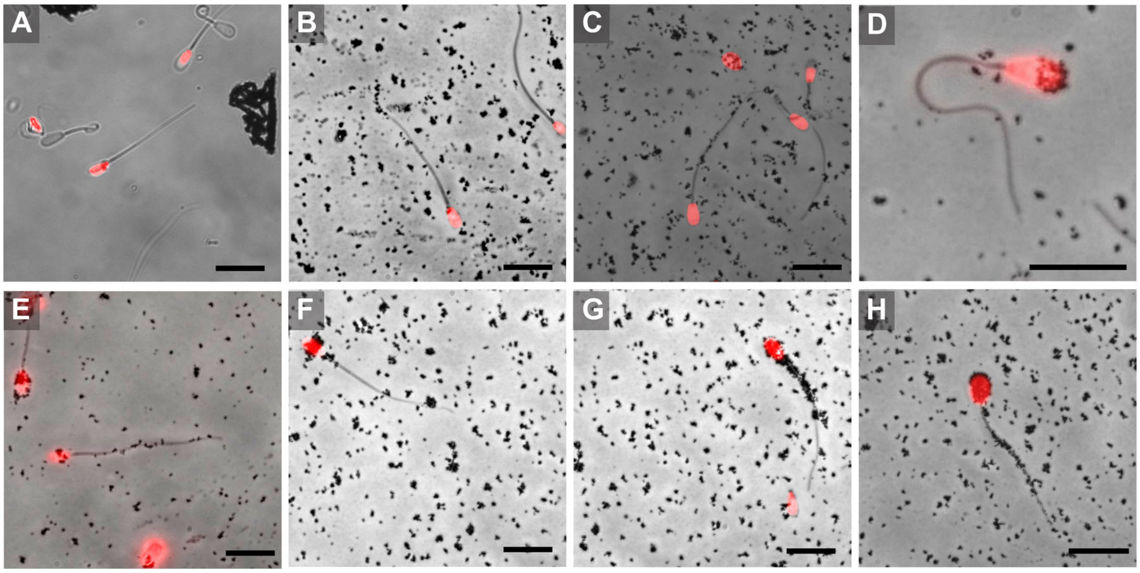

**Fig. 3** Microscopic images of different cases of particle attachment to bovine sperm. The cell heads are fluorescently labelled in red for better visibility and imaged in phase contrast/fluorescent microscopy. (A) Bovine sperm without particle attachment. (B) particle attached only on the distal end of the sperm flagellum. (C) particles in principal piece and distal end. (D) particles only on the acrosomal area of the head. (E) particles along the whole cell body. (F) particles on head and midpiece. (G) particles on midpiece and principal piece. (H) particles attached to head, midpiece and principal piece. Scale bars are 20 µm

electromagnetic-based excitation method. The bending stiffness was found to be increasing with the number and location of the magnetic particles attached to cellular segments[11]. Figure 3 illustrates different cases of IRONSperm with low particle coverage (Fig. 3B, C, D and F) on the tail, high coverage on the tail (Fig. 3E, G, F) or no bound particles (Fig. 3A). Note that the bovine sperm cells without any particles cannot be actuated by an external magnetic field. In the case of the sample shown in Fig. 3D with magnetic particle coverage only on the acrosomal area of the head, the resulting IRONSperm is soft exhibiting a transverse bending wave motion (Fig. 4A). In the case of the sample shown in Fig. 3G or H, the resulting samples is a relatively rigid IRONSperm performing rotational motion (see also motion in Fig. 4B). The time-dependent deformation of IRONSperm was measured and characterized in our previous study [27]. Another factor that has been reported to influence the bending stiffness of sperm flagella is the Adenosine triphosphate (ATP) content[20]. The molecular dynein motors located along the axoneme of the sperm tail display a 9+2 configuration. When the dynein arms bind ATP as their energy supply unit, it results in a bending motion of the microtubuli filament. In fact, the flagellum becomes more flexible when the a greater amount of ATP is bound to the cell membrane. [20]. Even if we consider in this study dead sperm cells that have been washed with distilled water before particle binding, the ATP that has been bound to the dynein motors previously will most likely not be released. This means that the resulting IRONSperm stiffness is also predominated by the cell's historical ATP content. The ATP content of the sperm cell is regulated by its metabolic processes such as glycolysis and oxidative phosphorylation that provide the cell with ATP on demand.

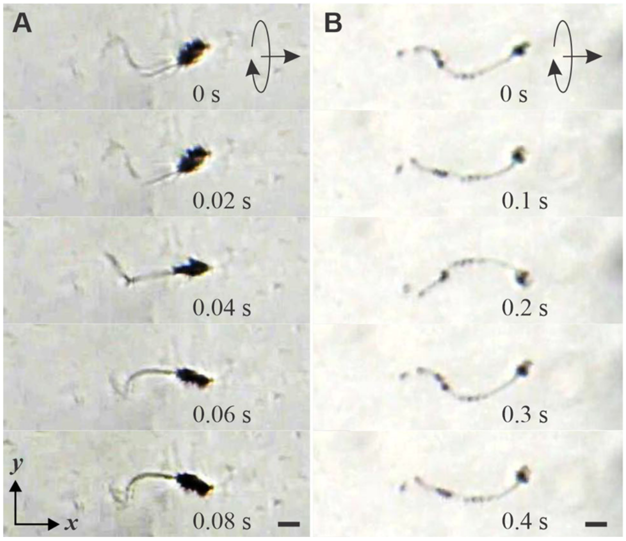

**Fig. 4** Soft (A) and rigid (B) IRONSperm samples swim by drag-based propulsion using an external rotating magnetic field with a field rotation-axis along the direction of motion. (A) A proximal-coated IRONSperm swims by passively propagating waves initiated from the rotation of the head. (B) The bending stiffness of a fully-coated IRONSperm is much greater than any other partially-coated cell and it is likely to undergo rigid-body rotations about its long axis. Scale bars are 10 µm

## 3 Drag-based thrust of flagellum with intrinsic variable stiffness

When an IRONSperm of bending stiffness $\kappa$ and total length $L$ is submerged in a viscous fluid and is subject to an external rotating magnetic field $\mathbf{B}(t)$, it will move using drag-based propulsion attributed to propagating transverse waves (Fig. 4(A)) along the length or rigid-body rotation with angular frequency $\omega = 2\pi f$ (Fig. 4(B)), where $f$ is the frequency of rotation.

### 3.1 Hydrodynamic drag force and torque

The bending stiffness of the flagellum dictates the swimming mode of IRONSperm. In the case of a flexible flagellum that undergoes elastic bending deformations, the propulsion is established by the wave propagation. The time taken by a propagating wave to spread along the flagellum scales as $\xi_\perp L^4/\kappa$, where $\xi_\perp = 4\pi\eta/\left(\ln(L/r_\mathrm{f} + 0.193)\right)$ is the perpendicular drag coefficient of a flagellum with a radius $r_\mathrm{f}$ [18]. In a proximal- or distal-coated flagellum, the bending stiffness is likely to be dependent on the condition of the membrane resulting in lower values of $\kappa$. When the magnetizable nanoparticles are distributed along the length, their concentration affect the bending stiffness. For both cases, in low-*Re* we have proportionality between the bending moment $\mathbf{M}$ and the change in curvature $\mathbf{K} - \mathbf{K_0}$

$$\mathbf{M} = \kappa\left(\mathbf{K} - \mathbf{K_0}\right), \tag{1}$$

leading to

$$\frac{\zeta_\perp}{\kappa}\frac{\partial \mathbf{r}}{\partial t} = \frac{\partial^4}{\partial s^4}\left(\mathbf{r} - \mathbf{r}_0\right), \tag{2}$$

where $\mathbf{K}(s, t)$ is the curvature vector derived from $\mathbf{r}(s, t)$, the position vector of points along the centerline of the flagellum with respect to a frame of reference (Fig. 1). The centerline is parameterized by the arclength $s$, $0 \le s \le L$. When the flagellum is bent into a curved circular shape, the initial configuration is characterized by $\mathbf{r}_0 = \mathbf{r}(s, 0)$ and initial curvature $\mathbf{K_0}$. Note that the elastohydrodynamics of the flagellum is nondimensionalized by $\kappa/L^2$, and the dimensionless sperm-compliance number $\mathcal{L}$ is given by [23, 24]

$$\mathcal{L} = L\left(\frac{\xi_\perp \omega}{\kappa}\right)^{1/4}. \tag{3}$$

The contribution of the bending stiffness, $\kappa$, to the sperm-compliance number allows the elastohydrodynamics described by Equations (1) and (2) to capture the two swimming modes. If the flagellum is rigid, $\mathcal{L} \ll 1$, then the left-hand side in Equation (2) vanishes, $\mathcal{L}\partial\mathbf{r}/\partial t \approx 0$. By integrating the right-hand side of Equation (2) over $s$, we can expect $\mathbf{r}(s, t)$ to be identically equal to $\mathbf{r}_0(s, 0)$ on the interval $s \in [0, L]$. Now consider the same flagellum, but with lower value of $\kappa$, resulting in greater values of $\mathcal{L}$ for the same geometric, $L$, rheological, $\xi_\perp$, and actuation, $\omega$, parameters. In this case, a magnetically-induced bending in shape spreads along the length at a rate proportional to $1/\kappa$. Therefore, we can use Equations (1) and (2) to capture two swimming modes of rigid and flexible IRONSperm by calculating $\mathbf{r}(s, t)$ for a range of $\kappa$.

Consider a rigid flagellum bent into a circular segment and a flexible flagellum characterized by $\mathbf{r}(s, 0)$ and $\mathbf{r}(s, t)$, respectively. The local velocity components along the flagellum are $\mathbf{v}_\| = [\dot{\mathbf{r}}\cdot\mathbf{t}]\mathbf{t}$ and $\mathbf{v}_\perp = \dot{\mathbf{r}} - \mathbf{v}_\|$ along the local tangent, $\mathbf{t}$, and normal directions to the centerline, respectively [25]. The relation between the hydrodynamic drag force density, $\mathbf{f}(s, t)$, and the velocity components is linear, we obtain [26]

$$\mathbf{f}(s, t) = \xi_\perp \mathbf{v}_\perp(s, t) + \xi_\| \mathbf{v}_\|(s, t), \tag{4}$$

where $\xi_\|$ is the parallel fluid dynamic resistance coefficient. Since IRONSperm is freely swimming, the total hydrodynamic drag force and moment balance are given by

$$\mathbf{F}_\mathrm{h}(t) + \int_0^L \mathrm{d}s\,\mathbf{f}(s, t) = 0. \tag{5}$$

Here $\mathbf{F}_\mathrm{h} = 6\pi a\mathbf{C}\mathbf{v}_\mathrm{h}$ is the viscous drag force of the head of length $2a$ and velocity $\mathbf{v}_\mathrm{h}$ (Fig. 1(A)), where $\mathbf{C}$ is a matrix of resistive coefficients. Note that unlike the flagellum, the head contributes drag but not thrust and the swimming speed can be determined using the force balance (5) regardless of the initial shape of the rigid flagellum or the stiffness of the flexible flagellum. The proximal coating is likely to play a role in the viscous drag by increasing the size (i.e., $2a$). The hydrodynamic drag moment balance is given by

$$\mathbf{M}_\mathrm{m}(t) + \mathbf{M}_\mathrm{h}(t) + \int_0^L \mathrm{d}s\,\mathbf{f}(s, t) \times \mathbf{r}(s, t) = 0, \tag{6}$$

where $\mathbf{M}_\mathrm{h}$ is the drag moment on the head and $\mathbf{M}_\mathrm{m}$ is the external magnetic torque. Equations (5) and (6) complete the hydrodynamics of IRONSperm and the instantaneous linear and angular velocities can be determined for a given bending stiffness, $\kappa$, and the contribution of the magnetic torque can be entered into the moment balance (6) using $\mathbf{M}_\mathrm{m}(t) = \mathbf{m}_\mathrm{h} \times \mathbf{B}(t)$. The imposed magnetic moment from a rotating magnetic field about the field-rotation axis, $\widehat{\boldsymbol{\omega}}_\mathrm{m}$, allows a rigid IRONSperm to undergo rigid-body rotation, while a soft IRONSperm would deform differently at different frequencies allowing 3-D helical waves to propagate.

### 3.2 Numerical simulation of the swimming path

Numerical calculations of the swimming behavior are implemented for one configuration of magnetic torque with field-rotation axis along $x$-axis, i.e. $\widehat{\boldsymbol{\omega}}_{\mathrm{m}} = \widehat{\boldsymbol{i}}$ and $\mathbf{B}(t) = B_x\widehat{\boldsymbol{i}} + B_{\mathrm{rot}}\cos(\omega t)\widehat{\boldsymbol{j}} + B_{\mathrm{rot}}\sin(\omega t)\widehat{\boldsymbol{k}}$ in the coordinate system depicted in Fig. 1. The component of magnetic field along $x$-axis is $B_x$ and $B_{\mathrm{rot}}$ is the rotating magnetic field component perpendicular to the $x$-axis. The magnetic torque is produced using a rotating magnetic field at 45° with $\widehat{\boldsymbol{i}}$-direction. The geometrical and rheological characteristics of the numerical scheme are fixed such that the influence of the swimming behavior is influenced only by the bending stiffness and initial deformation. Note that the proximal coating is likely to yield lowest bending stiffness as the flagellum is fully free of nanoparticles. In this case the energy is fed in by the magnetic torque acting only on the head and its magnitude is limited by the area of the negatively-charged regions. The amount of particles, and therefore the magnetic moment increases with the charged surface area. The surface area of the head is proportional to square of head radius, whereas the surface area of the flagellum is proportional to tail length, $L$, and tail diameter. Overall, the surface area of a sperm head is approximately twice as large as surface area of flagellum.

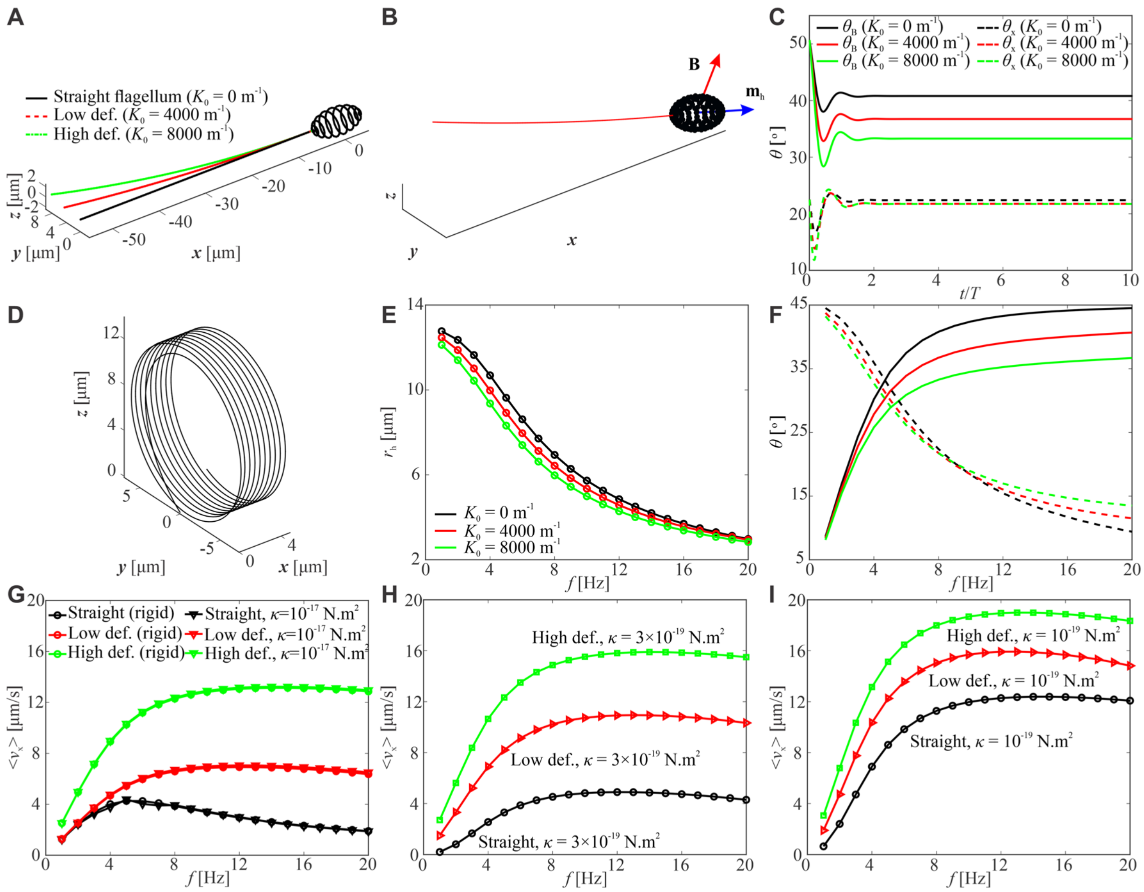

**Fig. 5** Simulation of movement for different initially-deformed IRONSperm under external rotating magnetic field is calculated using equations (1), (5) and (6). (A) Initial shape of IRONSperm with straight (black, curvature $K_0 \to \infty$), low deformation (red, circle with curvature $K_0 = 4000$ m$^{-1}$) and high deformation (green, $K_0 = 8000$ m$^{-1}$). (B) Low deformed IRONSperm during rotation with magnetic field vector $\mathbf{B}$ (red arrow) and magnetic moment vector $\mathbf{m}_{\mathrm{h}}$ (blue arrow). (C) Angles $\theta_B$ between magnetic moment $\mathbf{m}_{\mathrm{h}}$ and magnetic field $\mathbf{B}$ (solid) and angle $\theta_x$ between magnetic moment $\mathbf{m}_{\mathrm{h}}$ and the $\boldsymbol{x}$-axis (dashed) stabilize after 20 cycles $T = 20$ ($f = 8$ Hz, $\kappa \to \infty$). (D) The head follows a helical trajectory under the influence of a rotating field after a stabilizing time of $T = 20$ cycles. (E) The diameter of the circular trajectory, $2r_{\mathrm{h}}$, decreases with the actuation frequency regardless of initial flagellum deformation and bending stiffness. (F) Angle $\theta_{\mathrm{B}}$ increases and $\theta_x$ decreases with increasing frequency $f$ ($\kappa \to \infty$). (G) The time-averaged translational velocity $\langle v_x \rangle$, along the $\boldsymbol{x}$-axis is calculated over one period of rotation at each actuation frequency, $f$. Translational velocity over frequency for rigid flagellum (circles, $\kappa \to \infty$) and highly-rigid flagellum (triangles, $\kappa = 10^{-17}$ N.m$^2$). Translational velocity and step-out frequency of a initially-deformed IRONSperm is greater than that of an initially-straight IRONSperm. For $\kappa = 10^{-17}$ N.m$^2$, IRONSperm behaves like a rigid rod for all initial deformations. (H) Translational velocity of flexible IRONSperm ($\kappa = 3 \times 10^{-19}$ N.m$^2$). (I) Translational velocity of flexible IRONSperm ($\kappa = 10^{-19}$ N.m$^2$). As IRONSperm becomes more flexible ($\kappa$ decreases), the translational velocity increases and the influence of initial deformation on translational velocity becomes completely negligible

Therefore, the magnetic moment of the head is greater than that of the flagellum. For both cases (i.e., rigid and soft), the magnitude of the moment is roughly constant.

Finite difference method is used to solve equations (1), (5) and (6) for each frequency using alignment of magnetic moment with head axis, i.e., $\mathbf{m_h}{=}m_\mathrm{h}\hat{\mathbf{e}}_1$, $\hat{\mathbf{e}}_1{=}\frac{\mathrm{d}\mathbf{r}}{\mathrm{d}s}|_{s=0}/|\frac{\mathrm{d}\mathbf{r}}{\mathrm{d}s}|_{s=0}|$, bending moment $\mathbf{M}(s,t)=\int_s^L \mathrm{d}s\mathbf{f}(s,t)\times\mathbf{r}(s,t)$ and boundary condition of moment free distal end, i.e., $\mathbf{M}(s,t)|_{s=L}=0$. The initial shape is either a straight filament (i.e., $\mathbf{r}_0=0$, $\mathbf{K_0}=0$), a circular segment of low deformation (i.e., $\mathbf{K_0}=4000\ \mathrm{m}^{-1}$) or a circular segment of high deformation (i.e., $\mathbf{K_0}=8000\ \mathrm{m}^{-1}$) (Fig. 5A). With the field-rotation axis aligned along the $\boldsymbol{x}$-axis and the field being allowed to rotate at $f\in[1,20]$ Hz, the position of the head is calculated during drag-based propulsion for the soft and rigid flagellum. Figure 5B shows the head and flagellum together with magnetic field vector and magnetic moment vector at a frequency of $f=8$ Hz. Both the angle of the head relative to the $\boldsymbol{x}$-axis, $\theta_x$, and the angle between head axis and magnetic field, $\theta_\mathrm{B}$, change with time, reaching constant values after a few periods, $T=1/f$ (Fig. 5C). Then the trace of the head (Fig. 5D) follows a perfect, stable helix after a few periods. The radius of the helix $r_\mathrm{h}$ is shown in Fig. 5E and decreases with the increasing frequency because at lower frequencies, IRONSperm can conduct more movements than at higher frequencies. This simulation result shows that the amplitude of the head trajectory decreases as the actuation frequency increases regardless of the initial deformation. In addition, the amplitude of the head is greater for flagellum with lower deformation/curvature. Furthermore, the angle $\theta_x$ decreases as the frequency increases, which is opposite to the behavior of increasing angle $\theta_\mathrm{B}$ as the frequency increases. The angle $\theta_\mathrm{B}$ is low at low frequencies because the head can follow the magnetic field easily, but at increasing frequencies $\theta_\mathrm{B}$ increases. Finally, average velocity $\langle v_x\rangle$ is shown in Fig. 5G-I, for bending stiffness of $\kappa\to\infty$ and $\kappa=10^{-17}$ N.m$^2$ (Fig. 5G), $\kappa=3\times10^{-19}$ N.m$^2$ (Fig. 5H) and $\kappa=1\times10^{-19}$ N.m$^2$ (Fig. 5I). For $\kappa\to\infty$, only eq. (5) and (6) were solved. Since the curves of $\kappa\to\infty$ and $\kappa=10^{-17}$ N.m$^2$ are almost identical, it can be concluded that $\kappa=10^{-17}$ N.m$^2$ is still a rigid flagellum (Fig. 5G). Translational velocity increased with higher initial deformation and as the flagellum becomes more flexible. The rigid, straight flagellum show a sharper peak of translational speed than the flat peaks of deformed initial shape of any bending stiffness and the straight deformable flagellum cases.

In the case of a straight soft and a straight rigid flagellum with bending stiffness of $\kappa=2\times10^{-19}$ N.m$^2$ and $\kappa\to\infty$, respectively, the head follows a helix so that the trace is a circle in the $\boldsymbol{y}$-$\boldsymbol{z}$ plane. The wave-pattern does not visibly depend on the length (size) of the head ($2a$) for a given actuation frequency, as shown in Fig. 6(A-C). However, bending amplitude of the wave-pattern exhibits an decrease with the bending stiffness, leading to significantly different frequency response and swimming speeds (Fig. 6(D)). The instantaneous angular velocities of the soft and rigid IRONsperm indicate that their behavior to a rotating magnetic field is sim-

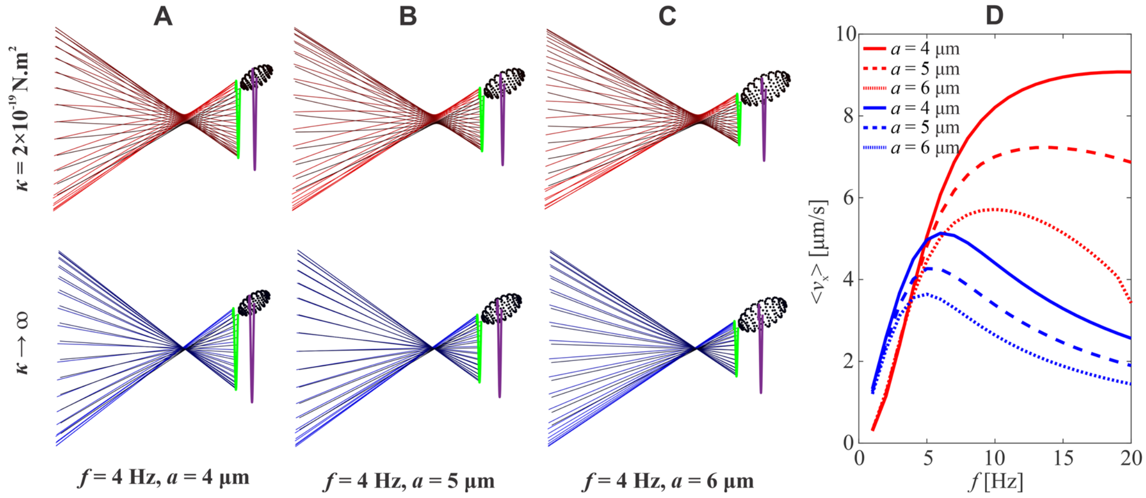

**Fig. 6** Wave-pattern and swimming speed are calculated for actuation frequency $f\in[1,20]$ Hz, sperm head length $2a=8,\ 10,\ 12$ μm, bending stiffness $\kappa=2\times10^{-19}$ N.m$^2$ and $\kappa\to\infty$ and initial curvature $K_0=0$ (straight). The curves represent the flagellum at equal time intervals over one beat cycle and the darker curves indicate later times. (A)-(C) The wave-pattern does not depend on the size of the head and the flagellum is straight for high bending stiffness and exhibits greater bending amplitude for lower bending stiffness. The violet and green curves represent the position of the head and the proximal end of the flagellum over one period. (D) The time-averaged swimming speed, $\langle v_x\rangle$, decreases with size of the sperm head and the bending stiffness. Proximal coating is likely to increase the length of the head, leading to drag but no thrust

ilar (Fig. 7(A)). Note that unlike the angular velocity case, the translational velocity of the soft IRONSperm is greater than that of the rigid IRONSperm, as shown in Fig. 7(B). Note that the swimming speed is measured for IRONSperm with proximal coating and approximately full coating, which, when combined provides more accurate behavior because of the nonuniform distribution of the nanoparticles along the flagellum. These two groups are combined as the bending stiffness of each flagellum has not been characterized. It has been shown that the bending stiffness can be estimated using wireless magnetic-based methods, resulting in an efficient tool to separate the samples based on their bending stiffness. However, it is not possible to use the same samples for motion control characterization because the wireless magnetic-based methods depend on fixing the proximal end and measuring the response of the distal end during excitation.

For both cases (proximal or fully coated), the time-averaged translational velocity, $\langle v_x \rangle$, increases below the step-out frequency and decreases approximately linearly on $f$. Measurements of the swimming speed of proximal-coated and fully coated IRONSperm samples are shown in Fig. 7(B) using the black curve ($n = 22$). We do not observe close quantitative agreement between the measured frequency response and the numerical results. However, the measured frequency response is bounded by the predicted frequency response of the rigid and flexible IRONSperm. Note that the shading represent the standard deviation of the measured swimming speed, and we attribute the large

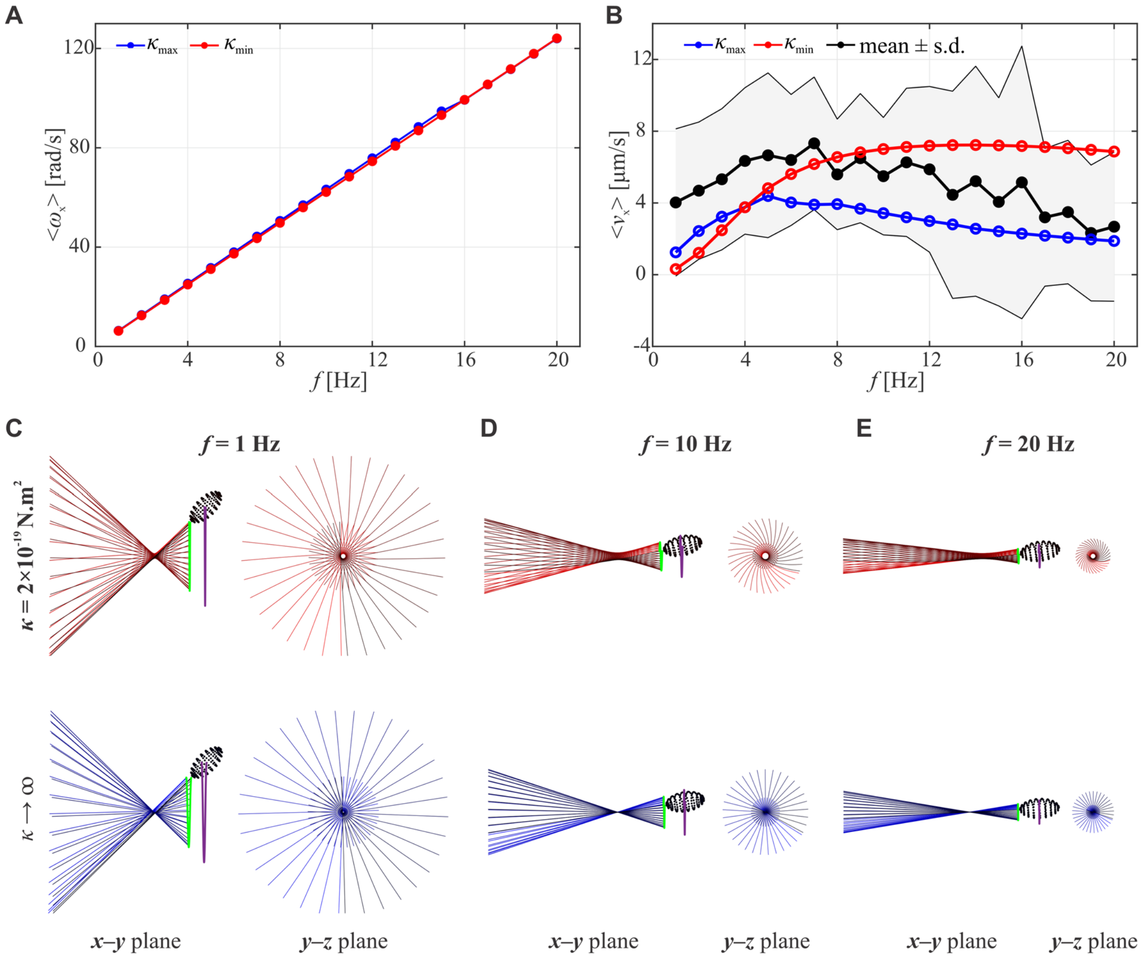

**Fig. 7** Frequency response of an initially-straight, flexible (red), $\kappa_{\min} = 2 \times 10^{-19}$ N.m$^2$, and rigid (blue), $\kappa_{\max} \rightarrow \infty$, IRONSperm is calculated using equations (1), (5) and (6). The time-averaged angular $\langle \omega_x \rangle$ and translational speeds $\langle v_x \rangle$, along the $\boldsymbol{x}$-axis are calculated over one period of rotation at each actuation frequency, $f$. (A) Rotational speed of flexible and rigid IRONSperm over rotating frequency. (B) Translational speed over frequency for flexible (blue), rigid (red) and mean (experimental results of IRONSperm with a range of nanoparticle coating). The step-out frequency of a rigid IRONSperm is smaller than that of a flexible IRONSperm. For a rigid IRONSperm, $\langle v_x \rangle$ increases and falls off gradually with the frequency. (C)-(E) IRONSperm with flagellum of bending stiffness $\kappa = 2 \times 10^{-19}$ N.m$^2$ (top) and $\kappa \rightarrow \infty$ (bottom) exhibits approximately similar wave-patterns with a decreasing envelope of motion for the increasing $f$ from 1 Hz (left) to 20 Hz (right). Decreasing $\kappa$ of the flagellum allows deformation regardless of $f$. The violet and green curves represent the position of the head and the proximal end of the flagellum over one period

**Table 1** Geometric, magnetic, and structural parameters of the numerical simulation

| Parameter | Value | Parameter | Value |
|---|---|---|---|
| $L$ [µm] | 60 | $r_{\mathrm{f}}$ [µm] | 0.5 |
| $2a$ [µm] | 10 | $2b$ [µm] | 5 |
| $B_x$ [mT] | 1 | $B_{\mathrm{rot}}$ [mT] | 1 |
| $m_{\mathrm{h}}$ [A.m$^2$] | $1.1 \times 10^{-12}$ | $\eta$ [mPa.s] | 0.7 |
| $f$ [Hz] | $1 - 20$ | $\kappa$ [N.m$^2$] | $1 - 3 \times 10^{-19}$, $10^{-17}$, rigid |
| $K_0$ [1/m] | 0, 4000, 8000 | $\langle q_{\mathrm{s}}(s) \rangle$ | $< 0$ |

IRONSperm consists of a flagellum of length $L$ and radius $r_{\mathrm{f}}$, and a head of length $2a$ and diameter $2b$. The rotating magnetic field is constructed using $B_x$ and $B_{\mathrm{rot}}$, and the induced magnetic moment, $m_{\mathrm{h}}$, allows IRONSperm to trail behind at frequency, $f$. $\eta$, $\kappa$, and $K_0$ represent the viscosity of the surroundings, bending stiffness and initial curvature of the flagellum, respectively

standard deviation to cell-to-cell variations in the charge distribution along the flagellum. The measured swimming speeds of the two groups are closely predicted using the model on average Table 1.

There is a noticeable difference between the drag-based propulsion using rigid-body rotation and transverse bending waves throughout the frequency range; although the geometrical, rheological, and magnetic characteristics are related. The physical reasons are the following: (a) when the flagellum is fully coated with nanoparticles (almost rigid) and its chiral shape is less dependent on frequency (Fig. 7(C)-(E)), portions of the flagellum will contribute drag and others will contribute thrust. Consider, for example, the $1 \leq f \leq 20$ Hz range for the rigid IRONSperm, the translational speed depends nonlinearly on $f$, although the rotational velocity increases linearly with $f$. (b) a proximal-coated flagellum (flexible) deforms and its shape depends on the frequency (Fig. 7(C)-(E)). In this case, all portions of the flagellum contribute to generating propulsion while the magnetizable head contributes drag.

## 4 Conclusions

When magnetizable nanoparticles are electrostatically assembled around the organic body of sperm cells, the resulting biohybrid microrobots (i.e., IRONSperm) will likely possess high flexibility or rigidity based on their original biochemical composition in terms of the cholesterol levels and other biomolecular contents of the membrane. The sperm membrane is particularly diverse compared to other cells due to the major remodelling process it undergoes during the maturation process.The sperm membrane carries a majority of negative surface charges. When cholesterol is embedded in the membrane prior to maturation of the sperm, it shifts the sperm charges to less negativity. Once the cholesterol is released, the overall charge of the sperm membrane reduces again to a larger presence of negative potential of the sperm membrane. The cholesterol content of the membrane directly affects the membrane fluidity, integrity, and surface charge, and thereby also affecting the bending stiffness of IRONSperm, as discussed in this manuscript. Additionally, we point out that the ATP content of the cell affects the bending stiffness. ATP molecules that bind to the molecular dynein motors hinder the dynein motors to bind to microtubule inside the sperm tail, which, in turn, reduces the stiffness of the flagellum. We show that in the limits of small and large bending stiffness (originating from the membrane composition, ATP content and/or the nanoparticle coating) two drag-based propulsion modes can be observed. In the first mode, swimming is achieved by rigid-body rotation and the frequency response depends on the initial curved shape that is formed after self-assembly. The second mode depends on propagating bending waves from the proximal end toward the distal end. Overall, it can be concluded that soft or curved IRONSperm actuation results in higher swimming speeds, which is advantageous for cargo transport. In addition, flexibility of the microrobots is advantageous when moving through tight spaces like channels or cavities. Nanoparticles have various effects on the sperm. They change elastic constants, friction constants and magnetic response. The effect of distributed magnetic moments from magnetic nanoparticles could be considered as additional magnetic moments in future numerical studies. The effect on overall bending stiffness was discussed in Ref. [11] In future studies, the maturation state of the spermatozoa will be controlled by inducing capacitation by incubation with maturation chemicals, e.g., heparin, bovine serum albumine or progesterone, and thereby obtain a certain cohort of sperm cells with specific membrane charge. Further, the bending stiffness of the sperm tails can be attempted to be tuned by controlling the ATP availability to the cells and hence reducing or increasing the stiffness. This article emphasizes the importance of physical and biochemical peculiarities of biohybrid microrobots that should be taken into account for microrobot design, fabrication, precision control and actuation.

**Author Contributions** V.M. conducted the biological study on spermatozoa and magnetically functionalized sperm. AK, LA and IK created

the mathematical model of IRONSperm of different bending stiffness. AK, IK and VM prepared the figures. All authors wrote and reviewed the manuscript.

**Funding** V. M. acknowledges the La Caixa Foundation (grant 100010434) for funding. This work was supported by the Faculty of Engineering Technology, University of Twente, under Grant Crazy-Research-2022.

**Availability of data and materials** Additional data are available upon request from the authors.

## Declarations

**Competing interests** The authors declare no competing financial or personal interests.

## References

1. Nelson BJ, Kaliakatsos IK, Abbott JJ (2010) Microrobots for minimally invasive medicine. Annu Rev Biomed Eng 12:55–85
2. Sitti M, Ceylan H, Hu W, Giltinan J, Turan M, Yim S, Diller E (2015) Biomedical applications of untethered mobile milli/microrobots. Proc IEEE Inst Electr Electron Eng 103:205–224
3. Zhang L, Petit T, Lu Y, Kratochvil BE, Peyer KE, Pei R, Lou J, Nelson BJ (2010) Controlled propulsion and cargo transport of rotating nickel nanowires near a patterned solid surface. ACS Nano 4:6228–6234
4. Kummer MP, Abbott JJ, Kratochvil BE, Borer R, Sengul A, Nelson BJ (2010) OctoMag: an electromagnetic system for 5-DOF wireless micromanipulation. IEEE Trans Robot 26:1006–1017
5. Behkam B, Sitti M (2007) Bacterial flagella-based propulsion and on/off motion control of microscale objects. Appl Phys Lett 90:023902
6. Magdanz V, Gebauer J, Mahdi D, Simmchen J, Khalil ISM (2019) In: International conference on manipulation, automation and robotics at small scales (MARSS). pp. 1–6
7. Reid AT, Redgrove K, Aitken RJ, Nixon B (2011) Cellular mechanisms regulating sperm-zona pellucida interaction. Asian J Androl 13:88–96
8. Huang X, Jain PK, El-Sayed IH, El-Sayed MA (2008) Plasmonic photothermal therapy (PPTT) using gold nanoparticles. Lasers Med Sci 23:217–28
9. Yan X, Zhou Q, Vincent M, Deng Y, Yu J, Xu J, Xu T, Tang T, Bian L, Wang Y-XJ, Kostarelos K, Zhang L (2017) Multifunctional biohybrid magnetite microrobots for imaging-guided therapy. Sci Robot 2:eaaq1155
10. Na HB, Song IC, Hyeon T (2009) Inorganic nanoparticles for MRI contrast agents. Adv Mat 21:2133–2148
11. Dias JMS, Estima D, Punte H, Klingner A, Marques L, Magdanz V, Khalil ISM (2022) Modeling and characterization of the passive bending stiffness of nanoparticle-coated sperm cells using magnetic excitation. Adv The Sim 5:2100438
12. Magdanz V, Vivaldi J, Mohanty S, Klingner A, Vendittelli M, Simmchen J, Misra S, Khalil ISM (2021) Impact of segmented magnetization on the flagellar propulsion of sperm-templated microrobots. Adv Sci 8:2004037
13. Teves ME, Roldan ERS (2021) Sperm bauplan and function and underlying processes of sperm formation and selection. Physiol Rev 102(1):7–60
14. Gao W, Feng X, Pei A, Kane CR, Tam R, Hennessy C, Wang J (2014) Bioinspired helical microswimmers based on vascular plants. Nano Lett 14:305–310
15. Kamata K, Piao Z, Suzuki S, Fujimori T, Tajiri W, Nagai K, Iyoda T, Yamada A, Hayakawa T, Ishiwara M, Horaguchi S, Belay A, Tanaka T, Takano K, Hangyo M (2015) Spirulina-templated metal microcoils with controlled helical structures for THz electromagnetic responses. Sci Rep 4:4919
16. Gilbert D, Ehrenstein G (1984) Membrane surface charge. Squid Axon 22:407–421
17. Klausen LH, Fuhs T, Dong M (2016) Mapping surface charge density of lipid bilayers by quantitative surface conductivity microscopy. Nat Commun 7:12447
18. Brennen C, Winnet H (1977) Fluid mechanics of propulsion by cilia and flagella. Ann Rev Fluid Mech 9:339–398
19. Magdanz V, Gebauer J, Sharan P, Eltoukhy S, Voigt D, Simmchen J (2019) Sperm-particle interactions and their prospects for charge mapping. Adv Biosys 3:1900061
20. Okuno M, Hiramoto Y (1979) Direct measurements of the stiffness of echinoderm sperm flagella. J Exp Biol 79:235–243
21. Magarkar A, Dhawan V, Kallinteri P, Viitala T, Elmowafy M, Róg T, Bunker A (2014) Cholesterol level affects surface charge of lipid membranes in saline solution. Sci Rep 4:5005
22. Lesich KA, de Pinho TG, Dang L, Lindemann CB (2014) Ultrastructural evidence that motility changes caused by variations in ATP, Mg2+, and ADP correlate to conformational changes in reactivated bull sperm axonemes. Cytoskeleton 71:649–661
23. Yu TS, Lauga E, Hosoi AE (2006) Experimental investigations of elastic tail propulsion at low Reynolds number. Phys Fluids 18:091701
24. Gadelha H (2013) On the optimal shape of magnetic swimmers. Regular Chaotic Dynamics 18:75–84
25. Friedrich BM, Riedel-Kruse IH, Howard J, Jülicher F (2010) High-precision tracking of sperm swimming fine structure provides strong test of resistive force theory. J Exp Biol 213:1226–1234
26. Rodenborna B, Chena C-H, Swinneya HL, Liub B, Zhang HP (2013) Propulsion of microorganisms by a helical flagellum. Proc Natl Acad Sci U S A 110:E338–E347
27. Magdanz V, Khalil ISM, Simmchen J, Furtado GP, Mohanty S, Gebauer J, Xu H, Klingner A, Aziz A, Medina-Sánchez M, Schmidt OG, Misra S (2020) IRONSperm: sperm-templated soft magnetic microrobots. Sci Adv 6:eaba5855

## Authors and Affiliations

**Veronika Magdanz**[1,2] · **Anke Klingner**[3] · **Leon Abelmann**[4,5] · **Islam S.M. Khalil**[6]

Anke Klingner
anke.klingner@guc.edu.eg

Leon Abelmann
l.abelmann@tudelft.nl

[1] Institute for Bioengineering of Catalonia (IBEC), Barcelona Institute of Science and Technology (BIST), Baldiri Reixac 10-12, Barcelona 08028, Catalonia, Spain

[2] Department of Systems Design Engineering, University of Waterloo, 200 University Ave W, Waterloo N2L 7, Ontario, Canada

[3] Department of Physics, German University of Cairo, New Cairo 11835, Egypt

[4] MESA+ Research Institute, University of Twente, Street, Enschede 7500 AE, The Netherlands

[5] Department of Microelectronics, Delft University of Technology, 2600 AA Delft, The Netherlands

[6] Department of Biomechanical Engineering, University of Twente, Enschede 7500 AE, The Netherlands